ATLAS NOTE

ATLAS-CONF-2016-110

28th September 2016

Study of photon-jet momentum correlations in Pb+Pb and *pp* collisions at $\sqrt{s_{\mathrm{NN}}}$ = 5.02 TeV with ATLAS

The ATLAS Collaboration

Abstract

Measurements of the azimuthal opening angle and transverse momentum balance between isolated photons and inclusive jets are presented using 0.49 nb^{-1} of Pb+Pb collision data at $\sqrt{s_{\mathrm{NN}}} = 5.02$ TeV and 26 pb^{-1} of *pp* collision data at $\sqrt{s} = 5.02$ TeV with the ATLAS detector at the LHC. Photons are required to have transverse momentum $60 < p_{\mathrm{T}}^{\gamma} < 200$ GeV and pseudorapidity $|\eta^{\gamma}| < 2.37$ (excluding the region $1.37 < |\eta^{\gamma}| < 1.52$), and to satisfy identification and isolation requirements. Jets are clustered from energy deposits in the calorimeter using the anti-k_t algorithm with parameter $R = 0.4$, and are required to have $p_{\mathrm{T}} > 30$ GeV and $|\eta| < 2.1$. Photons are paired inclusively with all jets in the event, and the transverse momentum balance of the pairs with azimuthal opening angle $\Delta\phi > 7\pi/8$ is studied. The jet-to-photon p_{T} ratio, $x_{\mathrm{J}\gamma}$, measured in data, is compared to that of simulated photon+jet events. In *pp* collisions, the distributions are well described by Monte Carlo simulation. In Pb+Pb collisions, the $x_{\mathrm{J}\gamma}$ distribution is observed to be modified with respect to the simulation in a way that is systematic in centrality and p_{T}^{γ}, in a manner consistent with the picture of parton-energy loss in the hot nuclear medium.

ATLAS-CONF-2016-110
30 September 2016

1. Introduction

Jet production in nucleus–nucleus collision events with a prompt photon with high transverse momentum (p_{T}) offers a useful way to understand the energy loss of fast partons that traverse the hot, deconfined medium created in these collisions [1–4]. At leading order in quantum chromodynamics (QCD), the photon and the jet are produced back-to-back in the azimuthal plane, with equal transverse momenta. Measurements of prompt photon production in Au+Au collisions at the Relativistic Heavy Ion Collider (RHIC) [5] and Pb+Pb collisions at the Large Hadron Collider (LHC) [6] have confirmed that, since photons are not strongly interacting, their production rates are unmodified by the medium [7]. Thus, photons provide an estimate of the kinematics of the parton produced in the initial hard-scattering before it has lost energy through interactions with the medium. Measurements of jet production under different selections on the photon kinematics can therefore shed light on how parton energy loss depends on the initial parton p_{T}. Furthermore, at fixed jet p_{T}, jets produced angularly opposite to the prompt photon are more likely to originate from quarks than those produced in dijet events. Thus, when considered together with measurements of inclusive jet production rates [8] or of the dijet p_{T} balance [9,10] in Pb+Pb collisions, analysis of photon+jet events can help constrain the flavor (*i.e.* quark versus gluon) dependence of parton energy loss.

Studies of photon–hadron correlations, in which high-p_{T} hadron fragments are used as a proxy for the jet, were first performed at RHIC [11,12]. Analyses of the angular and momentum correlations between photons and fully reconstructed jets have been performed by ATLAS and CMS in $\sqrt{s_{\mathrm{NN}}} = 2.76$ TeV Pb+Pb collision data [13,14]. In those studies, the distribution of the photon+jet azimuthal separation, $\Delta\phi$, was found to be unmodified with respect to simulated photon+jet events in a heavy-ion background, while the distribution of the jet-to-photon transverse momentum ratio, $x_{\mathrm{J}\gamma} = p_{\mathrm{T}}^{\mathrm{jet}}/p_{\mathrm{T}}^{\gamma}$, was significantly shifted to smaller values.

This note reports a study of photon+jet correlations in the $\sqrt{s_{\mathrm{NN}}} = 5.02$ TeV Pb+Pb and $\sqrt{s} = 5.02$ TeV pp collision data samples recorded in November and December 2015 with the ATLAS detector at the LHC, with integrated luminosities corresponding to 0.49 nb^{-1} and 26 pb^{-1}, respectively. The larger integrated luminosity with respect to previous LHC data, as well as the increased photon-production cross-sections at this collision energy, together allow for more differential studies of photon+jet angular and momentum correlations.

Events containing a prompt photon with $60 < p_{\mathrm{T}} < 200$ GeV and $|\eta| < 2.37$ (excluding the region $1.37 < |\eta| < 1.52$) are studied. Photons are paired with every jet in the event with $p_{\mathrm{T}} > 30$ GeV and $|\eta| < 2.1$. In Pb+Pb collisions, photon+jet pairs can be formed with jets from an unrelated hard scattering in the collision or from localised underlying event (UE) fluctuations reconstructed as jets. Furthermore, in both pp and Pb+Pb collisions, the experimentally selected photon sample contains a background admixture of non-isolated photons and neutral meson fragments from jets. After correcting for these backgrounds, the momentum balance of photon+jet pairs which are approximately angularly balanced, $\Delta\phi > 7\pi/8$, is analysed. The per-photon yield of jets as a function of $x_{\mathrm{J}\gamma}$ is studied for different selections on the photon p_{T} in pp collisions and for different selections on the centrality of the Pb+Pb collisions, which selects events with different degrees of nucleus–nucleus overlap. The background-corrected distributions in data are compared to the analogous quantities in simulated events which describe the effects of the heavy-ion background on the measured quantities but do not describe the physics of energy loss.

2. Experimental setup

The ATLAS experiment [15] is a multi-purpose particle detector with a forward-backward symmetric cylindrical geometry and nearly 4π coverage[1]. This analysis uses primarily the inner detector, the calorimeter and the trigger system.

The ATLAS inner detector comprises three major subsystems: the pixel detector, the semiconductor detector (SCT) and the transition radiation tracker (TRT), which cover full azimuth and pseudorapidity out to $|\eta| = 2.5$ and are immersed in a 2 T axial magnetic field. The pixel detector consists of four layers, at radii of 25.7, 50.5, 88.5 and 122.5 mm, arranged in cylindrical layers in the barrel region ($|\eta| < 2$) and three disks in the endcap region. The SCT comprises eight cylindrical layers of single-sided silicon strip detectors at radii ranging from 299 to 514 mm in the barrel region, and 9 disks in the endcap region. The transition radiation tracker (TRT) covers radii from 563 to 1066 mm and $|\eta| < 2$ and is divided into one barrel and two end-cap sections.

The ATLAS calorimeter is a large-acceptance, longitudinally segmented sampling detector covering $|\eta| < 4.9$ with electromagnetic (EM) and hadronic sections. The EM calorimeter is a lead/liquid-argon sampling calorimeter with an accordion-shaped geometry. It is divided into a barrel region, covering $|\eta| < 1.475$, and two endcap regions, covering $1.375 < |\eta| < 3.2$. The EM calorimeter has three primary sections, longitudinal in shower depth, called “layers”, in the barrel region and up to $|\eta| = 2.5$ in the endcap region. In the barrel and first part of the endcap ($|\eta| < 2.4$), with the exception of the regions $1.4 < |\eta| < 1.5$, the first layer has a fine segmentation in η ($\Delta\eta = 0.003$–0.006) to allow for the discrimination of photons from the two-photon decays of π^0 and η mesons. Over most of the acceptance, the total material upstream of the electromagnetic calorimeter ranges from 2.5 to 6 radiation lengths. In the transition region between the barrel and endcap regions ($1.37 < |\eta| < 1.52$), the amount of material rises up to 11.5 radiation lengths, and thus this region is not used for the photon measurement. The hadronic calorimeter section is located outside the electromagnetic calorimeter. It consists of a steel/scintillator sampling calorimeter situated at $|\eta| < 1.7$, a liquid-argon calorimeter with copper absorber situated at $1.5 < |\eta| < 3.2$, and a forward calorimeter (FCal) situated at $3.1 < |\eta| < 4.9$. The FCal is a liquid-argon sampling calorimeter located on either side of the interaction point, with each half composed of one electromagnetic and two hadronic sections, with copper and tungsten serving as the absorber material, respectively. The sum of the transverse energy in the cells in both modules is used to characterise the centrality of Pb+Pb collisions.

The ATLAS detector has a two-level trigger system, with a first-level trigger implemented in hardware to reduce the accepted event rate followed by a software-based (high-level) trigger. Data for this measurement were acquired using a high-level photon trigger [16] covering the central region ($|\eta| < 2.50$). At the first-level trigger stage, the transverse energy of electromagnetic showers is computed within a granularity of $\Delta\phi \times \Delta\eta = 0.2 \times 0.1$, and objects which satisfy an E_T threshold are used to seed the first step of the high-level trigger stage. At this next stage, reconstruction algorithms similar to those used in the offline analysis use the full detector granularity to form the final trigger decision. The trigger was configured with an online photon p_T threshold of 30 GeV and 20 GeV in the pp and Pb+Pb running, respectively, and required that the candidate passed a loose set of criteria on the electromagnetic shower shape. For the

---

[1] ATLAS uses a right-handed coordinate system with its origin at the nominal interaction point (IP) in the centre of the detector and the z-axis along the beam pipe. The x-axis points from the IP to the centre of the LHC ring, and the y-axis points upward. Cylindrical coordinates (r, ϕ) are used in the transverse plane, ϕ being the azimuthal angle around the z-axis. The pseudorapidity is defined in terms of the polar angle θ as $\eta = -\ln\tan(\theta/2)$. Transverse momentum and transverse energy are defined as $p_\mathrm{T} = p\sin\theta$ and $E_\mathrm{T} = E\sin\theta$, respectively. ΔR is defined as $\sqrt{(\Delta\eta)^2 + (\Delta\phi)^2}$.

Pb+Pb data-taking, the high-level trigger contains a version of the procedure used to estimate and subtract the UE contribution to the E_{T} measured in the calorimeter [6], ensuring that the efficiency remains high in high-activity Pb+Pb events.

In addition to the photon trigger, two triggers are used in Pb+Pb collisions to select minimum-bias events for the centrality analysis. These are based on the presence of a minimum amount of transverse energy in all sections of the calorimeter system ($|\eta| < 3.2$) or, for events which do not meet this condition, on the presence of substantial energy deposits in both zero-degree calorimeters (ZDCs), which are primarily sensitive to spectator neutrons in the region $|\eta| > 8.3$.

3. Data selection and centrality determination

Photon+jet events in Pb+Pb and *pp* collisions are initially selected for analysis by the high-level triggers described above. The presence of a reconstructed vertex in the inner detector is required in both datasets.

The centrality of Pb+Pb events is defined using the total transverse energy measured in the FCal, evaluated at the electromagnetic scale and denoted $\sum E_{\mathrm{T}}$, using the same definition as in the 2010 and 2011 Pb+Pb data at $\sqrt{s_{\mathrm{NN}}} = 2.76$ TeV [17]. The $\sum E_{\mathrm{T}}$ distribution for minimum-bias Pb+Pb events is selected for analysis using the minimum-bias triggers described above. An additional requirement, based on the correlation of the signals in the ZDC and the FCal, is used to reject a small amount of recorded events consistent with two Pb+Pb interactions in the same beam crossing.

The centrality determination for this dataset follows similar procedures to that used for lower-energy Pb+Pb data in ATLAS [17,18]. A Monte Carlo Glauber model simulation [19] with nucleon–nucleon cross-section $\sigma_{\mathrm{NN}} = 70$ mb is used to describe the distribution of Pb+Pb collision geometries at the underlying nucleon–nucleon level. The value of σ_{NN}, as well as the systematic variations in the Glauber model, are taken to be the same as that in the centrality analysis of *p*+Pb collisions at 5.02 TeV by ATLAS [20]. The $\sum E_{\mathrm{T}}$ distribution in Pb+Pb events of a fixed geometric configuration is taken to be a multiple convolution of the $\sum E_{\mathrm{T}}$ distribution in *pp* collisions. A two-component model [21] is used to hypothesize that the average level of particle production varies as a linear combination of the number of colliding (N_{coll}) and participating (N_{part}) nucleons, which represent the contributions to the signal from hard and soft particle production processes, respectively. Then, the hypothetical $\sum E_{\mathrm{T}}$ distribution for minimum-bias events is expressed as the sum of the $\sum E_{\mathrm{T}}$ distributions over the distribution of N_{coll} and N_{part} given by the Glauber model.

The hypothetical distribution is fit to the data in the region above $\sum E_{\mathrm{T}} = 40$ GeV, where the data were found to be free of electromagnetic Pb+Pb events and other processes which are not included in the Glauber model through an analysis of the pseudorapidity gap distributions in these events [22]. The fit was repeated by fixing different values of the two-component parameter x, while treating those describing the $\sum E_{\mathrm{T}}$ distribution for *pp* collisions as free parameters. The best fit was achieved with $x = 0.09$, consistent with that used in the 2.76 TeV centrality analysis, and indicates that 85% of the Glauber-like Pb+Pb distibution is contained above $\sum E_{\mathrm{T}} = 40$ GeV. Alternate choices of $x = 0.07, 0.11$ were motivated by an analysis of the $\sum E_{\mathrm{T}}$ distribution in *pp* data and by considering the largest deviation from the nominal value of 0.09 which still produced reasonable fits to the data. Under these variations, the fraction of the cross-section with $\sum E_{\mathrm{T}} > 40$ GeV changed by less than 1%. Minimum-bias Pb+Pb events above this value are divided into 85 percentiles containing equal numbers of events.

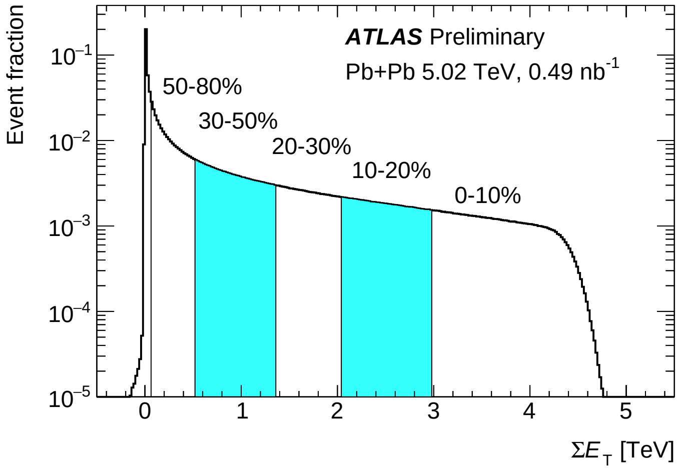

Figure 1: Measured $\sum E_{\mathrm{T}}$ distribution in minimum-bias Pb+Pb collisions at $\sqrt{s_{\mathrm{NN}}} = 5.02$ TeV. Alternating shaded and unshaded regions from the large-$\sum E_{\mathrm{T}}$ end of the distribution denote the 0–10%, 10–20%, 20–30%, 30–50% and 50–80% centrality ranges.

In this analysis, Pb+Pb events within four centrality ranges are considered: 0–10% (largest $\sum E_{\mathrm{T}}$ values and degree of nuclear overlap), 10–20%, 20–30%, 30–50% and 50–80% (smallest $\sum E_{\mathrm{T}}$ values and degree of nuclear overlap). Figure 1 shows the $\sum E_{\mathrm{T}}$ distribution in minimum-bias events and the ranges which correspond to these centrality selections.

Centrality range	$\sum E_{\mathrm{T}}$ range	N_{part}	N_{coll}	T_{AA} [mb^{-1}]
50–80%	0.0637-0.525 TeV	33.3 ± 1.5	48.3 ± 3.5	0.690 ± 0.046
30–50%	0.525–1.37 TeV	109.2 ± 2.5	265 ± 16	3.79 ± 0.13
20–30%	1.37–2.05 TeV	189.2 ± 2.8	6057 ± 38	8.64 ± 0.17
10–20%	2.05–2.99 TeV	264.1 ± 2.9	1003 ± 66	14.33 ± 0.18
0–10%	> 2.99 TeV	358.8 ± 2.3	1635 ± 114	23.35 ± 0.20

Table 1: Geometric parameters and systematic uncertainties in Pb+Pb data.

Mean values of N_{coll} and N_{part} are estimated for these selections, as well as the mean value of the nuclear overlap function $T_{\mathrm{AA}} = N_{\mathrm{coll}}/\sigma_{\mathrm{NN}}$. To determine a systematic uncertainty on these geometric parameters, the fit was repeated with variations in the two-component model parameter x by ±0.02 (which resulted in changes in the efficiency of ±1%). Variations in the Glauber modelling were used as in Ref. [20]: the nucleon–nucleon cross-section was varied by ±5 mb, and the Woods-Saxon parameters and minimum nucleon–nucleon distance were also varied. The results are shown in Table 1.

4. Monte Carlo simulation

Monte Carlo (MC) simulations of $\sqrt{s} = 5.02$ TeV *pp* photon+jet events were used to understand the performance of the ATLAS detector and provide the comparison distributions for those measured in *pp* and Pb+Pb collisions. The Pythia 8 generator [23] with parameters chosen to reproduce observables in data according to the A14 tune [24] and NNPDF23LO parton distribution function (PDF) set [25] was used to generate event samples with a generator-level photon in the p_{T} range from 50 GeV to 280 GeV. Samples corresponding to pp collisions were generated in this way and contained 6 million events.

Additionally, a separate sample of 18 million pp dijet events with the same generator, tune and PDF set was generated with different selections on the leading generator-level jet p_{T} to cover a wide range in jet p_{T}. This sample was used for the initial calibration of the detector response to jets, as described below.

Samples of photon+jet events in Pb+Pb collisions were generated in two variants. First, a sample of 6 million Pythia 8 photon+jet events was generated and overlaid with minimum-bias Pb+Pb data events recorded during the 2015 run. Second, a separate sample of 6 million events was overlaid using minimum-bias Pb+Pb events simulated with version 1.38b of the Hijing generator [26] with harmonic flow added to match previously measured flow harmonics.

For all the event samples described above, the simulated events were passed through a full Geant 4 simulation [27,28] of the ATLAS detector under the same conditions present during data-taking. During the analysis, the two Pb+Pb samples were reweighted at the event level such that their $\sum E_{\mathrm{T}}$ distribution matched that for the selected Pb+Pb events in data.

At the generator level, jets are defined by applying the anti-k_t algorithm [29] with $R = 0.4$ to stable particles[2] within $|\eta| < 4.9$.

5. Event reconstruction and performance

The procedures used for the reconstruction, selection and identification of isolated photons and for the reconstruction and calibration of hadronic jets are described in this section. They were applied identically to the experimental data and the MC simulation except where noted. The performance for photon and jet measurements in pp and Pb+Pb collisions was determined from the simulation samples.

5.1. Photon reconstruction and selection

The photon reconstruction and selection procedure follows that used by ATLAS for the previous measurement of prompt isolated photon production in Pb+Pb collisions [6]. The pile-up and UE contributions to the energy deposited in the calorimeter cells were estimated and subtracted on an event-by-event basis using the techniques developed for the reconstruction of jets in the dense heavy-ion environment [8]. The impact of both the average transverse energy in narrow η regions, and the local modulation in ϕ produced by the second (elliptic) term of the harmonic expansion of the azimuthally modulated underlying event, was removed from each event, leaving a set of “subtracted” cells.

Using the subtracted cells, photon and electron candidates were reconstructed from clusters of energy deposited in the electromagnetic calorimeter, primarily seeded in the second compartment with cells of granularity $\Delta\eta \times \Delta\phi \approx 0.025 \times 0.0245$. Since the inner detector tracking was constrained to a single vertex in Pb+Pb collisions, all photon candidates were classified as unconverted photons. However, those matched to a track consistent with originating from an electron produced in the beam interaction region

---

[2] Stable particles are defined as those with a proper mean lifetime, τ, exceeding $c\tau = 10$ mm. Muons and neutrinos from decaying hadrons are excluded from the jet clustering.

were classified as electrons and removed from the analysis. Only photon candidates with $|\eta| < 2.37$ were utilised in this analysis, and the transition region $1.37 < |\eta| < 1.52$ between the barrel and end-cap calorimeter was excluded. This is due to the reduced calorimeter granularity, as well as the presence of significant additional inactive material, which degrades the photon identification capabilities and energy resolution.

Photon identification was based primarily on shower shapes in the calorimeter, with the selection criteria optimised for the conditions expected for the 2015 proton-proton data. An initial loose selection was derived using only the information from the hadronic calorimeter and the lateral shower shape in the second layer of the electromagnetic calorimeter, which contains most of the energy. This was used primarily for the high-level trigger. The final ("tight") selection applies tighter criteria to a larger set of nine variables, in particular placing requirements on the shower shape in the finely segmented first calorimeter layer to reject the two-photon decay of neutral mesons. When applying the photon identification criteria to simulated events, the shower shapes were corrected for small differences in their average values between data and simulation.

To further reject the background from jets misidentified as photons, the photon candidates were required to be isolated using the information from the calorimeter. The isolation variable, $E_{\mathrm{T}}^{\mathrm{iso}}$, is defined using only information from the calorimeter as the sum of the E_{T} of cells subtended by a cone of size $\Delta R = 0.3$ around each photon candidate, excluding an area of size $\Delta\eta \times \Delta\phi \approx 0.125 \times 0.172$ centered on the photon cluster. The expected photon energy deposit outside the excluded area was subtracted. In Pb+Pb, the mean $E_{\mathrm{T}}^{\mathrm{iso}}$ after subtraction was then corrected for a residual linear dependence on $\sum E_{\mathrm{T}}$.

The final photon selection required candidates to pass the tight identification criteria and to be isolated according to $E_{\mathrm{T}}^{\mathrm{iso}} < 3$ GeV in *pp* collisions. In Pb+Pb collisions, where UE fluctuations significantly broaden the distribution of $E_{\mathrm{T}}^{\mathrm{iso}}$ values, this requirement was set at approximately one standard deviation of the Gaussian-like part of the distribution centered at zero, $E_{\mathrm{T}}^{\mathrm{iso}} < 8$ GeV. The selection efficiency for generator-level photons was $> 90\%$ in *pp* collisions. In Pb+Pb collisions, the efficiency decreased systematically in more central events due to a number of effects, including photons failing the isolation cut due to sitting atop an UE fluctuation, or by being tagged as electrons through a combinatoric pairing with a reconstructed track in the event. For 0–10% Pb+Pb collisions, the efficiency rose systematically with p_{T}, reaching 75% at $p_{\mathrm{T}}^{\gamma} = 150$ GeV. The total numbers of selected photons in each p_{T}^{γ} range and event type are given in Table 2.

In addition to this selection, a background-enhanced set of photon candidates which preferentially arise from neutral mesons in jets was selected by requiring that they fail at least one out of a set of four of the nine shower shape cuts (called "non-tight" cuts). Two additional sets of photon candidates were defined by applying tight or non-tight cut requirements, but requiring that the photons were not isolated such that $E_{\mathrm{T}}^{\mathrm{iso}} > 5$ GeV in *pp* collisions or > 10 GeV in Pb+Pb collisions. Figure 2 shows an example of $E_{\mathrm{T}}^{\mathrm{iso}}$ distributions in *pp* and Pb+Pb events, with the distribution for non-tight photon candidates normalised to give the same integral in the non-isolated region as the tight candidates.

The mean response in simulation for the measured photon p_{T} was found to be correct within 1%, and the p_{T} resolution was 3%. Both quantities were centrality-independent within uncertainties.

Dataset	$60 < p_{\mathrm{T}}^{\gamma} < 80$ GeV	$80 < p_{\mathrm{T}}^{\gamma} < 100$ GeV	$100 < p_{\mathrm{T}}^{\gamma} < 150$ GeV	$150 < p_{\mathrm{T}}^{\gamma} < 200$ GeV
pp	26564	7282	3898	556
50–80% Pb+Pb	1045	301	148	24
30–50% Pb+Pb	3668	956	539	73
20–30% Pb+Pb	3567	989	549	91
10–20% Pb+Pb	5071	1500	846	117
0–10% Pb+Pb	7375	2212	1313	172

Table 2: Tight, isolated photon counts in *pp* and Pb+Pb data for each p_{T}^{γ} selection.

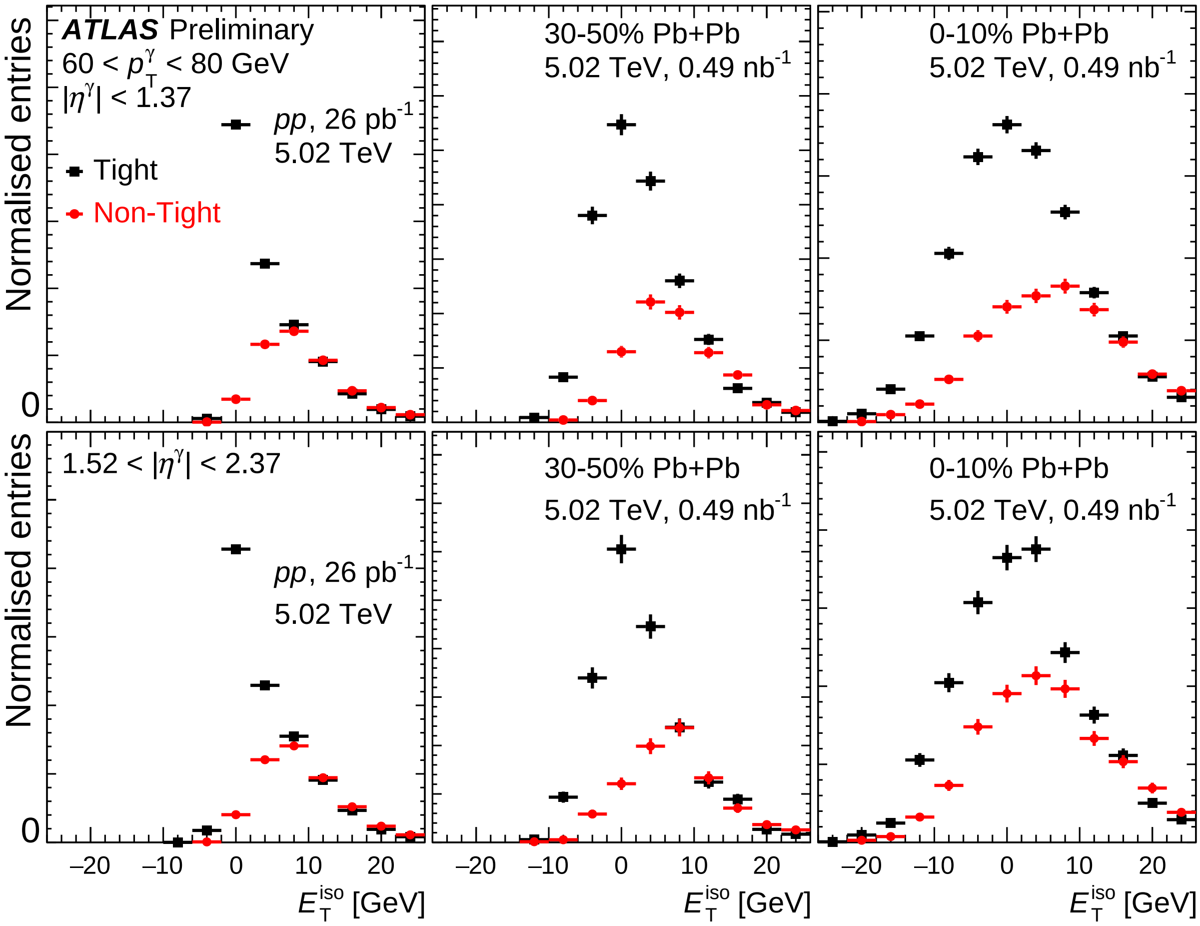

Figure 2: Distribution of the photon isolation transverse energies, $E_{\mathrm{T}}^{\mathrm{iso}}$, in *pp*, 30–50% and 0–10% Pb+Pb collisions for tight (black squares) and non-tight (red circles) selected photons, in the barrel (top row) and endcap (bottom row) regions of the electromagnetic calorimeter. Distributions are normalised to have the same integral at large $E_{\mathrm{T}}^{\mathrm{iso}}$ ($>$ 5 GeV and $>$ 10 GeV in *pp* and Pb+Pb collisions, respectively).

5.2. Jet reconstruction and calibration

The jet reconstruction and UE determination and subtraction procedures closely follow those used by ATLAS for jet measurements in *pp* and Pb+Pb collisions at $\sqrt{s_{\mathrm{NN}}} = 2.76$ TeV [30,31], and are summarised in Ref. [8]. Jets were reconstructed by applying the anti-k_t algorithm with $R = 0.4$ to energy deposits in the calorimeter grouped into towers of size $\Delta\eta \times \Delta\phi = 0.1 \times 0.1$. An iterative procedure was used to obtain an event-by-event estimate of the average η-dependent UE energy density, while excluding jets from that estimate. An updated estimate of the jet four-momentum was obtained by subtracting the UE energy from the constituent towers of the jet. This procedure was also applied to pp collisions, in which the UE subtraction removes the small energy density deposited from additional collisions in the same bunch crossing. The p_{T} of the resulting jets was corrected for the calorimeter energy response using an η- and p_{T}-dependent calibration derived from simulations of hard scattering pp events, described above in Sec. 4.

Then, an *in situ* correction, derived through studies of events with a jet recoiling against a photon or Z boson as part of the calibration for jets in $\sqrt{s} = 13$ TeV pp collisions [32] in ATLAS, was applied to correct for differences in the jet response between data and the MC sample. A separate cross-calibration, determined in $\sqrt{s} = 13$ TeV data, was applied to account for the differences between the heavy-ion reconstruction algorithm and that normally used in the 13 TeV data.

After this calibration sequence, the resulting energy scale for heavy-ion jets was experimentally validated by studying the photon+jet balance in data and simulated pp events, similarly to what was done by ATLAS for the heavy-ion jet reconstruction in lower-$\sqrt{s}$ pp data [33]. This study uses a set of selection requirements that is more stringent than that in the main analysis and is designed to pick out configurations in which the photon is balanced by only a single high-p_{T} jet. Figure 3 shows the average of the ratio between the leading jet p_{T} and the reference, $p_{\mathrm{T}}^{\mathrm{ref}} = p_{\mathrm{T}}^{\gamma}\cos(\Delta\phi)$, demonstrating that, after the *in situ* calibration is applied to the jets, data and simulation agree within the uncertainties of the cross-calibration procedure.

The jet reconstruction performance was studied in $p_{\mathrm{T}}^{\gamma} > 60$ GeV photon+jet events by comparing the transverse momentum $p_{\mathrm{T}}^{\mathrm{truth}}$ of generator-level jets which pass the analysis selection criteria ($p_{\mathrm{T}} > 30$ GeV, $|\eta| < 2.1$, $\Delta\phi > 7\pi/8$) to that of their associated reconstructed jets, $p_{\mathrm{T}}^{\mathrm{reco}}$. The mean response, defined as the mean of the $p_{\mathrm{T}}^{\mathrm{reco}}/p_{\mathrm{T}}^{\mathrm{truth}}$ distribution, was found to differ from unity by a few percent. This effect arises in part from the different flavor composition of the photon+jet sample and the dijet sample from which the calibration was derived, coupled with a residual flavor-dependent calorimeter response for low-p_{T} jets. To restore the mean response to unity, a calibration to account for these deviations was derived by examining the mean response. In pp collisions, the mean response was parameterised as a function of $p_{\mathrm{T}}^{\mathrm{jet}}$, while in Pb+Pb collisions, a single $p_{\mathrm{T}}^{\mathrm{jet}}$-independent calibration factor was used. This calibration was applied as a multiplicative factor to the p_{T} in data and simulation.

Figure 4 summarises two other aspects of the jet performance: the reconstruction efficiency and jet energy resolution, defined as the standard deviation of the response distribution. In the most central events, the reconstruction efficiency rises from 75% to 100% over the range $p_{\mathrm{T}} = 30$ GeV to $p_{\mathrm{T}} = 60$ GeV. The resolution systematically decreases with p_{T}, dropping to 10% for $p_{\mathrm{T}}^{\mathrm{jet}} = 150$ GeV in pp and 30–50% Pb+Pb collisions.

6. Data analysis

The set of photon+jet pairs in data contains a combinatoric contribution from the correlation of a high-p_{T} photon with jets unrelated to the photon-producing hard scattering (in Pb+Pb collisions) and from dijet pairs in which the photon or neutral meson in one of the jets has been erroneously selected as a

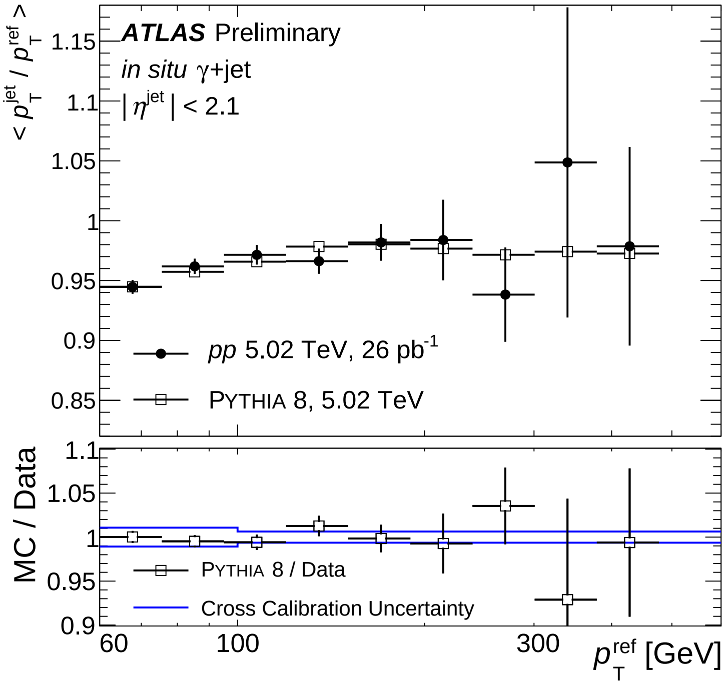

Figure 3: *Top panel:* photon+jet *in situ* transverse momentum balance in *pp* data (filled circles) and Pythia 8 simulation (open squares), as a function of $p_{\mathrm{T}}^{\mathrm{ref}} = p_{\mathrm{T}}^{\gamma} \cos(\Delta\phi)$ (see text). *Bottom panel:* Ratio of simulation to data (open squares). The horizontal band within the blue lines represents the component of the systematic uncertainty on the ratio corresponding to the cross-calibration of the heavy-ion jet energy scale to that for *pp* jet reconstruction.

prompt photon (in *pp* and Pb+Pb collisions). These backgrounds are subtracted from the data with two corrections that use data-driven methods. The corrections are performed separately for each p_{T}^{γ} selection and separately in *pp* collisions and Pb+Pb collisions of different centrality ranges.

While the details are described below, the final effect of both corrections on the $p_{\mathrm{T}}^{\mathrm{jet}}$ distributions in photon-selected 0–10% Pb+Pb events is illustrated in Figure 5. The combinatoric background contributes at low-p_{T} and is restricted primarily to $p_{\mathrm{T}} < 50$ GeV. It is also strongly centrality dependent, being nearly negligible in 30–50% collisions and largest in 0–10% collisions. The dijet background contributes to a broad range of $p_{\mathrm{T}}^{\mathrm{jet}}$ values, especially populating the region $p_{\mathrm{T}}^{\mathrm{jet}} > p_{\mathrm{T}}^{\gamma}$, since the p_{T} ratio of a jet to a neutral meson fragment in the balancing jet is likely to be above unity. This background has a similar shape in all selections. Since the photon purity is lower in Pb+Pb collisions than in *pp* collisions, the correction is larger for Pb+Pb.

6.1. Combinatoric background subtraction

Simulated photon+jet events overlaid with minimum bias Pb+Pb data are used to determine the combinatoric photon+jet background level. The reconstructed jets in each simulated event are classified as those which are angularly matched ($\Delta R < 0.4$) to a generator-level jet with $p_{\mathrm{T}} > 10$ GeV, and thus arise from the same hard scattering as the photon, or those which are not matched in this way and are thus consistent with arising from the original Pb+Pb data event. Per-photon $\Delta\phi$, $p_{\mathrm{T}}^{\mathrm{jet}}$, and $x_{J\gamma}$ distributions are determined with the set of reconstructed jets not matched to a generator-level jet. Since the simulated events are overlaid

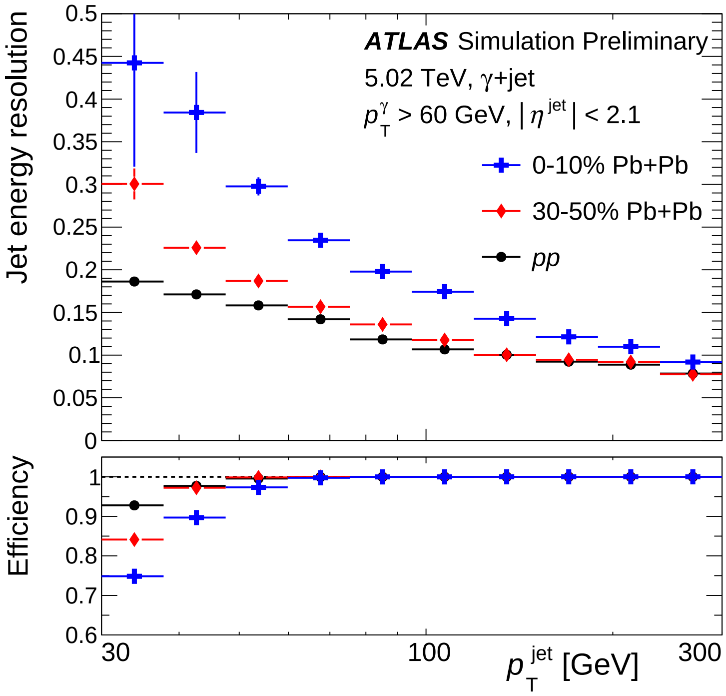

Figure 4: Jet energy resolution (top panel) and reconstruction efficiency (bottom panel) shown as a function of p_T for jets with $\Delta\phi > 7\pi/8$ in photon+jet events, in *pp* (black circles), 30–50% (red diamonds) and 0–10% (blue crosses) Pb+Pb collisions.

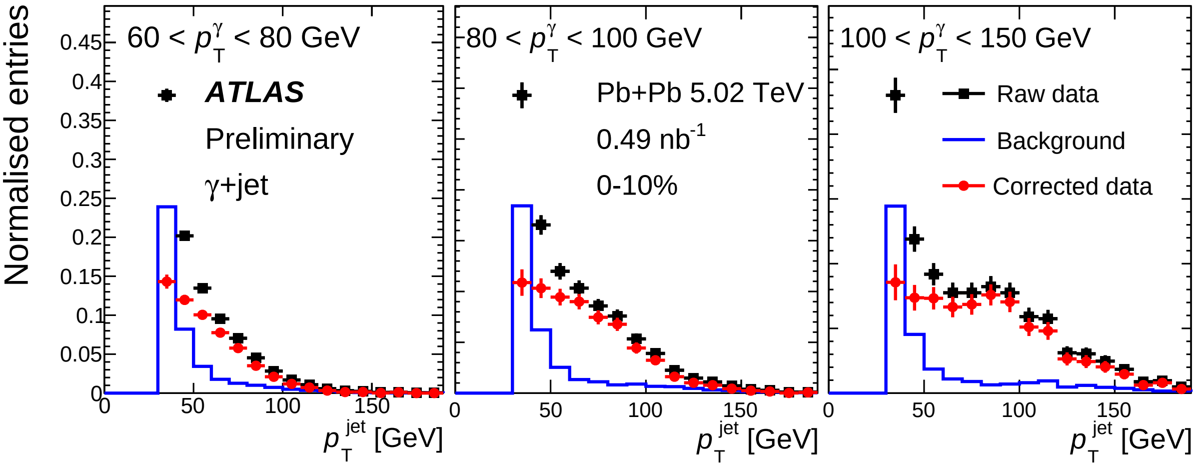

Figure 5: Illustration of background subtraction procedure. Each panel shows, for a different selection on p_T^γ, the jet yields as a function of p_T^{jet} in photon-selected 0–10% Pb+Pb events. Distributions are shown for jets in all selected photon events (black squares), the estimated background contribution (blue histogram), and background-subtracted distributions (red circles).

with Pb+Pb data, they contain the same statistical distribution of unrelated jets as do the photon+jet events in data, in addition to the same detector effects. The per-photon distributions for jets not matched to truth jets in the simulation are thus an estimate of the combinatoric photon+jet contribution, and are statistically subtracted from the per-photon distributions in data.

6.2. Dijet background subtraction

First, for each photon p_{T}^{γ} and event class, the purity of selected photons is determined with the double sideband approach used extensively for photon measurements in ATLAS [6]. In this approach, let A and B be the sidebands containing tight photons which are isolated and non-isolated, respectively, and let C and D be the sidebands containing non-tight photons which are isolated and non-isolated, respectively. Let $N_{\mathrm{A,B,C,D}}$ be the number of photon candidates in each sideband, which may generally be a mixture of signal and background photons. For background photons (those arising from neutral mesons inside jets), their $E_{\mathrm{T}}^{\mathrm{iso}}$ value is expected to be uncorrelated with whether they are tight or non-tight. This is due to the fact that non-tight photon candidates are selected by requiring them to fail identification cuts for shower shapes which are nominally uncorrelated with the isolation.

If all signal photons lie in sideband A, such that the photons in sidebands B, C and D are purely background, the yield of signal photons in region A could then be estimated in a straightforward way via $N_{\mathrm{A}} - N_{\mathrm{B}} N_{\mathrm{D}} / N_{\mathrm{C}}$. However, simulation studies show that the photon signal leaks into sidebands B, C and D, which requires a more careful treatment. In pp collisions, only a few percent of signal photons end up in sidebands B, C and D. In Pb+Pb collisions, this fraction is somewhat higher, in particular for generator-level isolated photons which end up in sideband B due to them sitting atop an upward, local fluctuation of the UE. Using this data-driven procedure and accounting for the leakage, the purity of the selected photons, defined as the ratio of the number of signal photons to all selected photons, can be determined. The purity grows systematically with p_{T}^{γ}. In pp collisions, it is $> 95\%$ at $p_{\mathrm{T}}^{\gamma} = 100$ GeV, while in Pb+Pb collisions it is typically ≈ 80–85% in this kinematic region.

Second, combinatoric-subtracted distributions in data are used to estimate the background from dijets. The per-photon distributions of $\Delta\phi$, $p_{\mathrm{T}}^{\mathrm{jet}}$, and $x_{\mathrm{J}\gamma}$ are constructed for photon candidates in sidebands C and D. These distributions are scaled to match the measured photon impurity, and are statistically subtracted from the signal distribution yields. The number of photon candidates in the signal selection is also corrected to account for this impurity.

6.3. Systematic uncertainties

After background subtraction, systematic uncertainties on the measured distributions have been estimated to account for several potential uncertainties, which can be categorised as arising from the uncertainty in the jet energy measurement, in the photon identification and energy measurement, and in the background subtraction procedure.

Five sources of uncertainty are related to the jet energy measurement. These are:

- The baseline uncertainty on jet energy measurements in pp collisions [34] is 5% for low jet-p_{T} and decreases systematically with p_{T}.
- A p_{T} and η-dependent uncertainty, typically 1%, is associated with the cross-calibration of the heavy-ion style jet reconstruction to that used for measurements in $\sqrt{s} = 13$ TeV pp collisions.
- The uncertainty on the jet energy resolution in pp collisions, determined through data-driven studies as in Ref. [35], is evaluated by applying an additional smearing of the jet p_{T} to increase the resolution, typically by a few percent.

- A combined uncertainty on the composition of jet flavor and the flavor-dependence of the jet response is used which is similar to that used for 13 TeV *pp* collisions but appropriate for collisions at 5.02 TeV. It is 2% at low-p_{T} and decreases systematically with p_{T}.
- An additional uncertainty for the jet energy scale in Pb+Pb collisions is estimated from studies of the charged-particle jet to calorimeter-jet momentum scale in simulation and data, of the response to quenched jets in simulation, and of the residual non-closure for low-p_{T} jets observed in simulation. It is 1% for $p_{\mathrm{T}} > 50$ GeV jets, but rises to 5–10% for $p_{\mathrm{T}} < 50$ GeV jets.

Four sources of uncertainty are related to the photon identification and measurement:

- The photon purities are varied by their statistical uncertainties, which are negligible in the $60 < p_{\mathrm{T}}^{\gamma} < 80$ GeV selection but rise to a few percent in the $100 < p_{\mathrm{T}} < 150$ GeV selection, and the dijet background subtraction is adjusted by this change in the purity.
- The experimental photon isolation requirement is raised by 2 GeV in *pp* and Pb+Pb collisions, resulting in an increased yield at the cost of a lower purity and larger dijet background contribution.
- Stricter and looser variations on the non-tight identification cuts designed to select dijet background candidates are considered, which change both the dijet background templates and estimated purities.
- An uncertainty on the photon energy measurement is estimated for 13 TeV collision data [36] and is typically smaller than 1%.
- The assumption that the distribution of background photons factorises along the identification and isolation axes was tested by varying the product $N_{\mathrm{B}}N_{\mathrm{C}}/(N_{\mathrm{A}}N_{\mathrm{D}}) = 1 \pm 0.2$ for background photons and repeating the purity calculation, as was performed in Ref. [6].

For the nominal combinatoric photon+jet correction, the $\sum E_{\mathrm{T}}$ distibution in the simulated data overlay samples is weighted to match that for selected photon events in data. This ensures that the estimate of the uncorrelated jet rate is appropriate for the data. As a conservative variation to test the sensitivity of this reweighting, the simulation is instead weighted to match the $\sum E_{\mathrm{T}}$ distribution for minimum bias Pb+Pb events, systematically decreasing the estimate of the combinatoric rate in all Pb+Pb selections.

To evaluate the sensitivity of the measurement to each of these effects, a variation to the analysis is applied from each source, and the resulting effects on the results are summed in quadrature to determine a total uncertainty. The total systematic uncertainty is determined by adding the uncertainty from each source in quadrature. In the range $x_{\mathrm{J}\gamma} < 1$, the relative uncertainty is typically 10–15%. For Pb+Pb events at very low values of $x_{\mathrm{J}\gamma}$, the uncertainty rises to 30–40%. In the range $x_{\mathrm{J}\gamma} > 1$, the relative uncertainty strongly increases, but the yield in that region is small.

7. Results

This section presents the background-corrected, measured distributions in data, which are compared to the analogous distributions in simulation.

Figure 6 compares the measured distributions in *pp* collisions to those made with the Pythia 8 generator. In *pp* collisions, the $x_{\mathrm{J}\gamma}$ distributions are peaked at ≈ 0.9, have a tail at larger values of $x_{\mathrm{J}\gamma}$, and feature a shoulder at smaller values of $x_{\mathrm{J}\gamma}$. The shape of the distribution at small $x_{\mathrm{J}\gamma}$ is in part a consequence

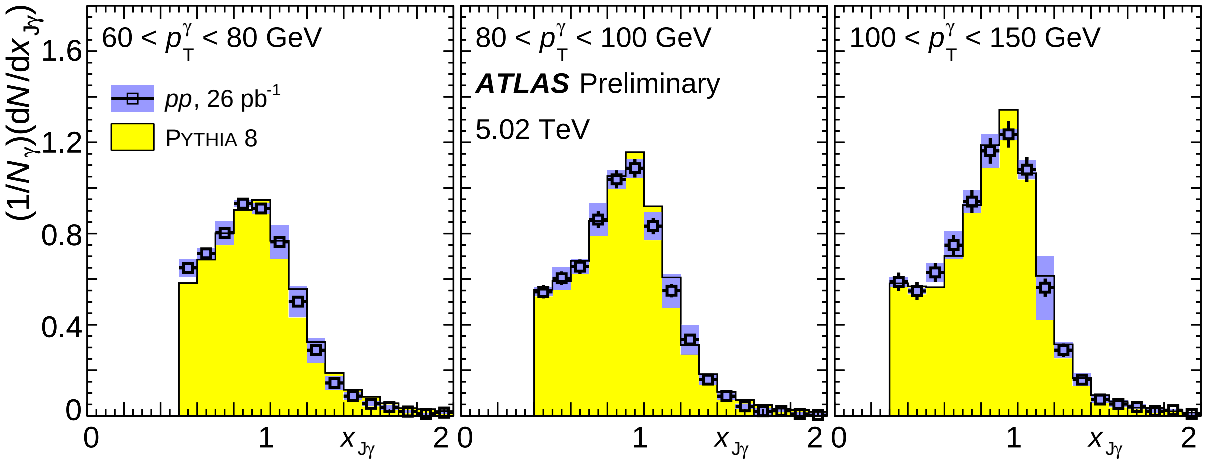

Figure 6: Measured distributions of the jet-to-photon transverse momentum ratio $x_{J\gamma}$ in *pp* collisions (open squares) and PYTHIA 8 simulation (yellow histogram). Each panel shows a different p_T^γ selection. The vertical bars and the shaded bands show the statistical and systematic uncertainties on the data, respectively.

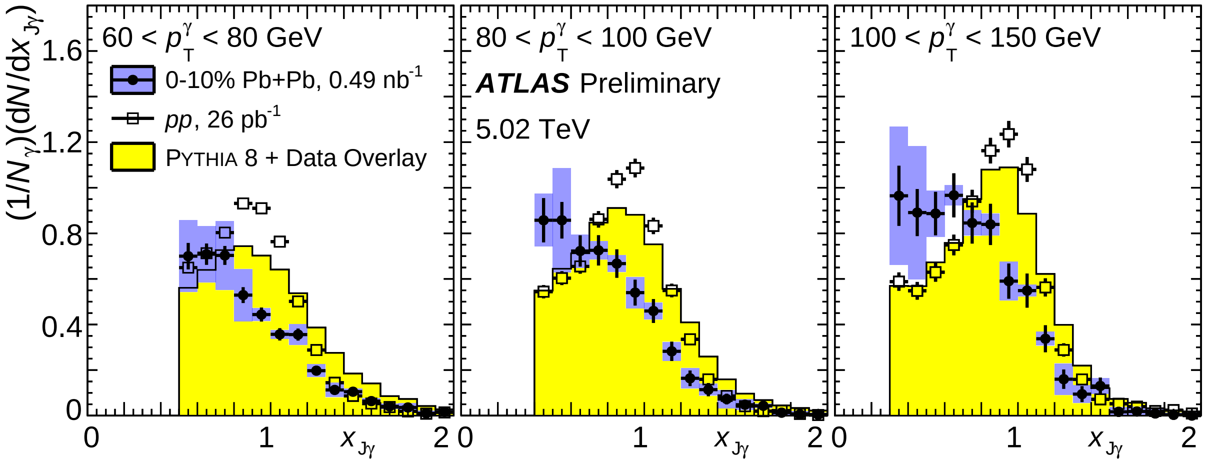

Figure 7: Measured distributions of the jet-to-photon transverse momentum ratio $x_{J\gamma}$ in 0–10% Pb+Pb collisions (filled circles), *pp* collisions (open squares) and PYTHIA 8 simulation overlaid with 0–10% Pb+Pb data (yellow histogram). Each panel shows a different p_T^γ selection.

of the fact that the photon is correlated with all the jets in the event that pass selection cuts inclusively (*i.e.* the correlation is not solely with the highest-p_T jet in the event, and no attempt is made to remove configurations where the photon is balanced by multiple high-p_T jets). The simulation is able to describe the shape and overall yield of the distributions in data in some detail.

Figure 7 compares the distributions in 0–10% Pb+Pb events to the simulated PYTHIA 8 photon+jet events overlaid with minimum bias Pb+Pb data. In each p_T^γ selection, the distributions in data are substantially modified with respect to the results of the simulation, in a manner that is consistent with a shift to lower values of $x_{J\gamma}$. The distributions have a different shape (they do not exhibit a clear peak within the visible $x_{J\gamma}$ range), and the integrated yield of associated jets above the minimum $x_{J\gamma}$ value is suppressed. This pattern of modification is indicative with a picture of parton-energy loss in the hot nuclear medium.

Figures 8, 9 and 10 explore the centrality dependence of the $x_{J\gamma}$ distributions in Pb+Pb data, each for

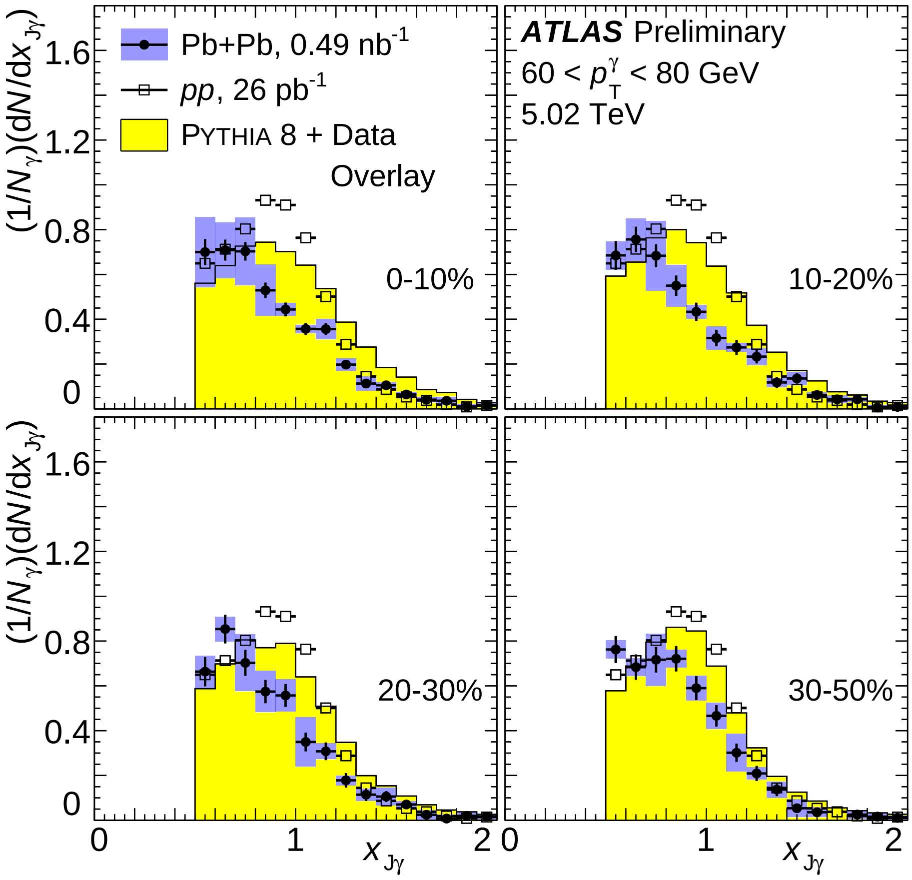

Figure 8: Measured distributions of the jet-to-photon transverse momentum ratio $x_{J\gamma}$ in $60 < p_T^\gamma < 80$ GeV events, comparing Pb+Pb data (filled circles), pp (open squares), and PYTHIA 8 simulation overlaid with Pb+Pb data (yellow histogram). Each panel shows a different selection on the Pb+Pb event centrality. The vertical bars and the shaded bands show the statistical and systematic uncertainties on the Pb+Pb data, respectively.

a single p_T^γ selection. In 0–10% collisions, the data is most different from the simulation. However, the distributions in data evolve in successively more peripheral event selections, and the distributions become systematically closer to those in simulation. In 30–50% Pb+Pb events, the distributions in data and simulation are notably closer together, and appear to have a non-trivial evolution with p_T^γ. For the $60 < p_T^\gamma < 80$ GeV selection, the $x_{J\gamma}$ distribution in 30–50% events is clearly modified. However, for the $100 < p_T^\gamma < 150$ GeV selection, the data is much closer to the simulation, suggesting that in photon+jet events, the fraction of energy lost may decrease with increasing parton p_T.

In addition to studies of the momentum correlation between the photon and associated jets, the azimuthal balance is also explored for $p_T^\gamma > 80$ GeV and $p_T^{\text{jet}} > 50$ GeV. Figure 11 compares the resulting $\Delta\phi$ distributions, normalised in the signal region $\Delta\phi > 7\pi/8$, between pp data and simulated photon+jet events. The simulation does not describe the data at low values of $\Delta\phi$, which may arise from the simulation containing a different relative contribution of direct and fragmentation photons (as investigated in Ref. [37]), or from the leading-order generator having an inadequate description of photon+multijet processes in this particular kinematic region.

Figure 12 compares the $\Delta\phi$ distributions in 0–10% Pb+Pb data and simulation, and in pp data. At values

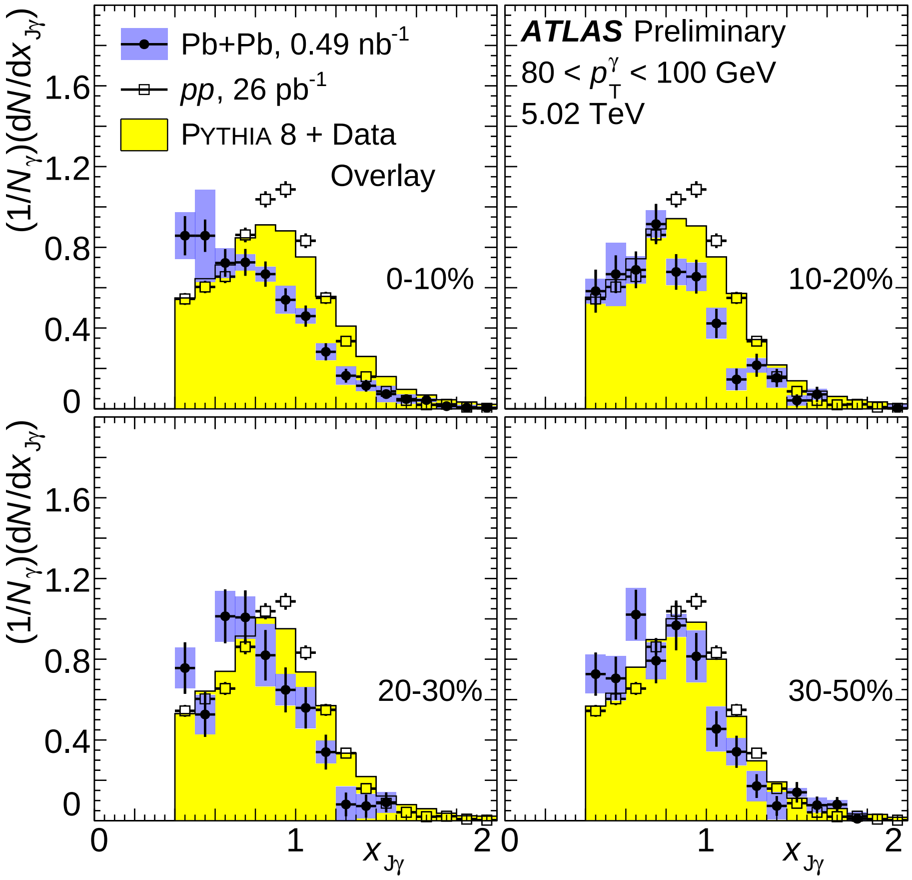

Figure 9: Measured distributions of the jet-to-photon transverse momentum ratio $x_{J\gamma}$ in $80 < p_T^\gamma < 100$ GeV events, comparing Pb+Pb data (filled circles), pp (open squares), and PYTHIA 8 simulation overlaid with Pb+Pb data (yellow histogram). Each panel shows a different selection on the Pb+Pb event centrality. The vertical bars and the shaded bands show the statistical and systematic uncertainties on the Pb+Pb data, respectively.

of $\Delta\phi \ll \pi$, the systematic uncertainties in the Pb+Pb data are large due to a number of sources, including uncertainties in the energy scale for low-p_T jets and those inherent in the background subtraction. Within the sensitivity of the measurement, the shape of the Pb+Pb data distribution is consistent with that in pp collisions and in the simulated Pb+Pb events.

8. Conclusions

This note presents a study of photon+jet angular and momentum correlations in $\sqrt{s_{NN}} = 5.02$ TeV Pb+Pb and pp events with $60 < p_T^\gamma < 200$ GeV photons. The data are corrected on a statistical level for the presence of combinatoric photon+jet pairs and of dijet pairs where one of the jets has been misidentified as a photon. The measured quantities in data are compared to the analogous quantities in simulated photon+jet events overlaid with minimum-bias Pb+Pb events. The per-photon distributions of the jet-photon p_T balance, $x_{J\gamma} = p_T^{\text{jet}}/p_T^\gamma$, for pairs with a back-to-back configuration, $\Delta\phi > 7\pi/8$, are observed to have a significantly modified total yield and shape in Pb+Pb collisions. These modifications are systematic in collision centrality and p_T^γ, consistent with the picture that the partons initially produced opposite to

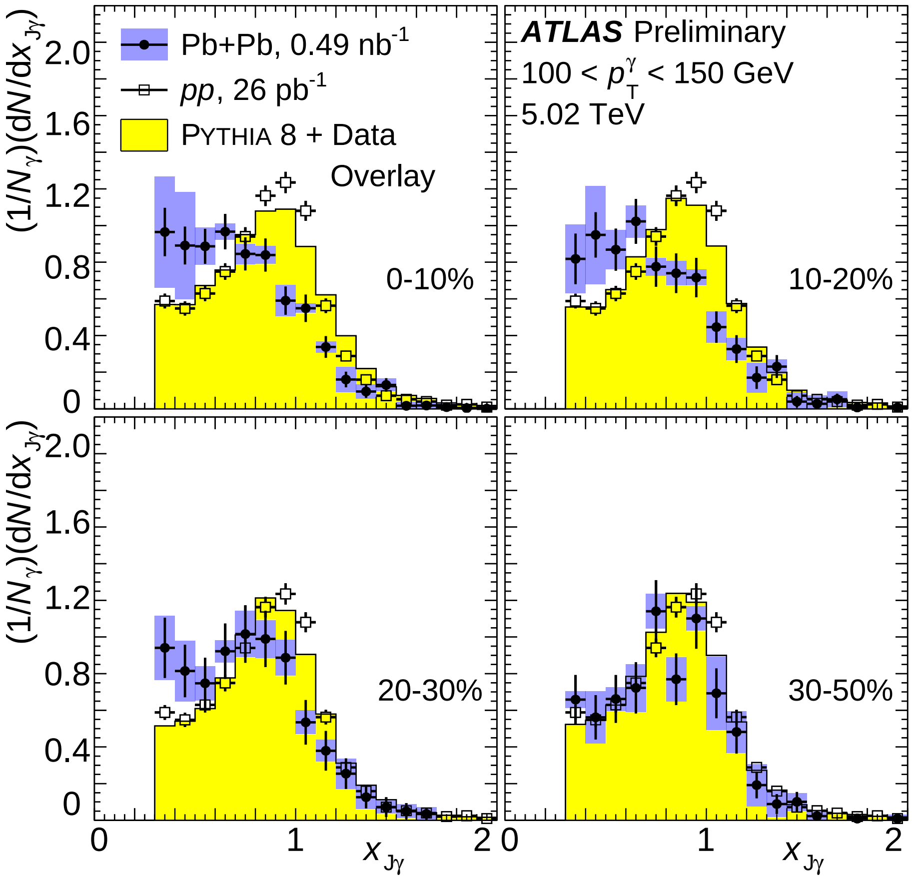

Figure 10: Measured distributions of the jet-to-photon transverse momentum ratio $x_{J\gamma}$ in $100 < p_T^\gamma < 150$ GeV events, comparing Pb+Pb data (filled circles), *pp* (open squares), and Pythia 8 simulation overlaid with Pb+Pb data (yellow histogram). Each panel shows a different selection on the Pb+Pb event centrality. The vertical bars and the shaded bands show the statistical and systematic uncertainties on the Pb+Pb data, respectively.

a high-p_T photon lose energy in their interactions with the hot nuclear medium but remain angularly well-correlated with the photon direction.

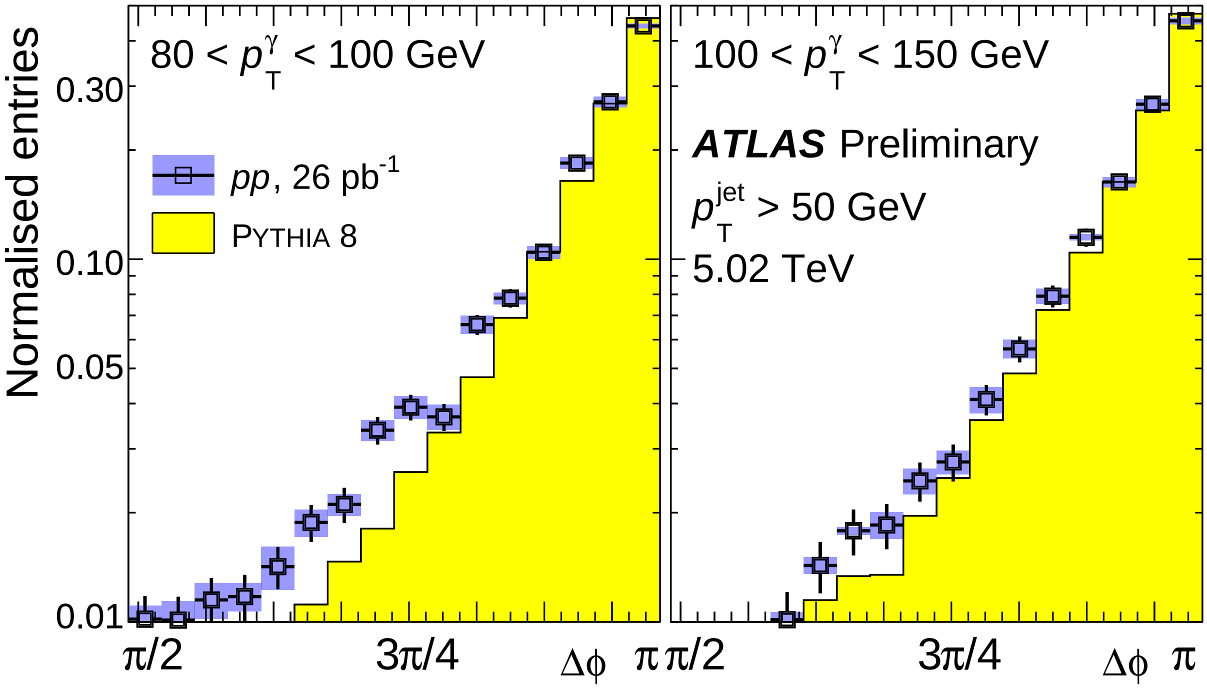

Figure 11: Distributions of the photon+jet azimuthal separation $\Delta\phi$ in pp collisions (open squares) and in the Pythia 8 simulation (yellow histogram). The distributions are normalised to have the same integral in the region $\Delta\phi > 7\pi/8$. Each panel shows a different p_T^γ selection. The vertical bars and the shaded bands show the statistical and systematic uncertainties on the data, respectively.

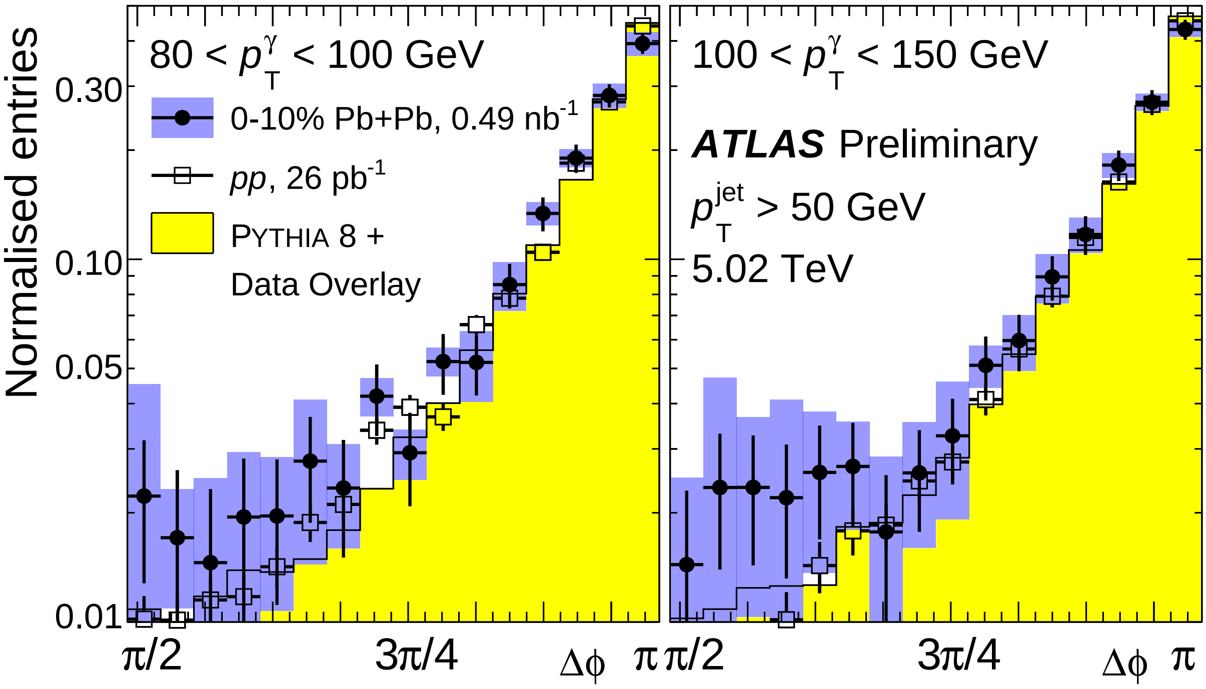

Figure 12: Distributions of the photon+jet azimuthal separation $\Delta\phi$ in 0–10% Pb+Pb collisions (filled circles), *pp* collisions (open squares) and Pythia 8 simulation overlaid with 0–10% Pb+Pb data (yellow histogram). The distributions are normalised to have the same integral in the region $\Delta\phi > 7\pi/8$. Each panel shows a different p_T^γ selection. The vertical bars and the shaded bands show the statistical and systematic uncertainties on the Pb+Pb data, respectively.

References

[1] G.-Y. Qin, Eur. Phys. J. C **74** (2014) 2959, `arXiv:1210.6610 [hep-ph]`.

[2] X.-N. Wang and Y. Zhu, Phys. Rev. Lett. **111** (2013) 062301, `arXiv:1302.5874 [hep-ph]`.

[3] W. Dai, I. Vitev, and B.-W. Zhang, Phys. Rev. Lett. **110** (2013) 142001, `arXiv:1207.5177 [hep-ph]`.

[4] J. Casalderrey-Solana, D. C. Gulhan, J. G. Milhano, D. Pablos, and K. Rajagopal, JHEP **03** (2016) 053, `arXiv:1508.00815 [hep-ph]`.

[5] PHENIX Collaboration, S. Afanasiev et al., Phys. Rev. Lett. **109** (2012) 152302, `arXiv:1205.5759 [nucl-ex]`.

[6] ATLAS Collaboration, Phys. Rev. C **93** (2016) 034914, `arXiv:1506.08552 [hep-ex]`.

[7] F. Arleo, K. J. Eskola, H. Paukkunen, and C. A. Salgado, JHEP **04** (2011) 055, `arXiv:1103.1471 [hep-ph]`.

[8] ATLAS Collaboration, Phys. Lett. B **719** (2013) 220, `arXiv:1208.1967 [hep-ex]`.

[9] ATLAS Collaboration, Phys. Rev. Lett. **105** (2010) 252303, `arXiv:1011.6182 [hep-ex]`.

[10] ATLAS Collaboration, ATLAS-CONF-2015-052, `http://cds.cern.ch/record/2055673`.

[11] PHENIX Collaboration, A. Adare et al., Phys. Rev. Lett. **111** (2013) 032301, `arXiv:1212.3323 [nucl-ex]`.

[12] STAR Collaboration, L. Adamczyk et al., Phys. Lett. B **760** (2016) 689–696, `arXiv:1604.01117 [nucl-ex]`.

[13] CMS Collaboration, Phys. Lett. B **718** (2013) 773–794, `arXiv:1205.0206 [nucl-ex]`.

[14] ATLAS Collaboration, ATLAS-CONF-2012-121, `http://cds.cern.ch/record/1473135`.

[15] ATLAS Collaboration, JINST **3** (2008) S08003.

[16] ATLAS Collaboration, ATL-DAQ-PUB-2016-001, `http://cds.cern.ch/record/2136007`.

[17] ATLAS Collaboration, Phys. Lett. B **707** (2012) 330–348, `arXiv:1108.6018 [hep-ex]`.

[18] M. L. Miller, K. Reygers, S. J. Sanders, and P. Steinberg, Ann. Rev. Nucl. Part. Sci. **57** (2007) 205–243, `arXiv:nucl-ex/0701025 [nucl-ex]`.

[19] C. Loizides, J. Nagle, and P. Steinberg, SoftwareX **1-2** (2015) 13–18, `arXiv:1408.2549 [nucl-ex]`.

[20] ATLAS Collaboration, Eur. Phys. J. C **76** (2016) 199, `arXiv:1508.00848 [hep-ex]`.

[21] X.-N. Wang and M. Gyulassy, Phys. Rev. Lett. **86** (2001) 3496–3499, `arXiv:nucl-th/0008014 [nucl-th]`.

[22] ATLAS Collaboration, Eur. Phys. J. C **72** (2012) 1926, `arXiv:1201.2808 [hep-ex]`.

[23] T. Sjöstrand, S. Mrenna, and P. Z. Skands, Comput. Phys. Commun. **178** (2008) 852, `arXiv:0710.3820 [hep-ph]`.

[24] ATLAS Collaboration, ATL-PHYS-PUB-2014-021, `http://cds.cern.ch/record/1966419`.

[25] S. Carrazza, S. Forte, and J. Rojo, *Parton Distributions and Event Generators*, in *Proceedings, 43rd International Symposium on Multiparticle Dynamics (ISMD 13)*. 2013. `arXiv:1311.5887 [hep-ph]`.

[26] W.-T. Deng, X.-N. Wang, and R. Xu, Phys. Rev. C **83** (2011) 014915, `arXiv:1008.1841 [hep-ph]`.

[27] GEANT4 Collaboration, S. Agostinelli et al., Nucl. Instrum. Meth. A **506** (2003) 250.

[28] ATLAS Collaboration, Eur. Phys. J. C **70** (2010) 823, `arXiv:1005.4568 [physics.ins-det]`.

[29] M. Cacciari, G. P. Salam, and G. Soyez, Eur. Phys. J. **C72** (2012) 1896, `arXiv:1111.6097 [hep-ph]`.

[30] ATLAS Collaboration, Phys. Rev. Lett. **114** (2015) 072302, `arXiv:1411.2357 [hep-ex]`.

[31] ATLAS Collaboration, Phys. Lett. B **748** (2015) 392, `arXiv:1412.4092 [hep-ex]`.

[32] ATLAS Collaboration, ATL-PHYS-PUB-2015-015, `http://cds.cern.ch/record/2037613`.

[33] ATLAS Collaboration, ATLAS-CONF-2015-016, `http://cds.cern.ch/record/2008677`.

[34] ATLAS Collaboration, Eur. Phys. J. C **75** (2015) 17, `arXiv:1406.0076 [hep-ex]`.

[35] ATLAS Collaboration, Eur. Phys. J. C **73** (2013) 2306, `arXiv:1210.6210 [hep-ex]`.

[36] ATLAS Collaboration, ATL-PHYS-PUB-2016-015, `http://cds.cern.ch/record/2203514`.

[37] ATLAS Collaboration, Nucl. Phys. B **875** (2013) 483–535, `arXiv:1307.6795 [hep-ex]`.

A. Appendix

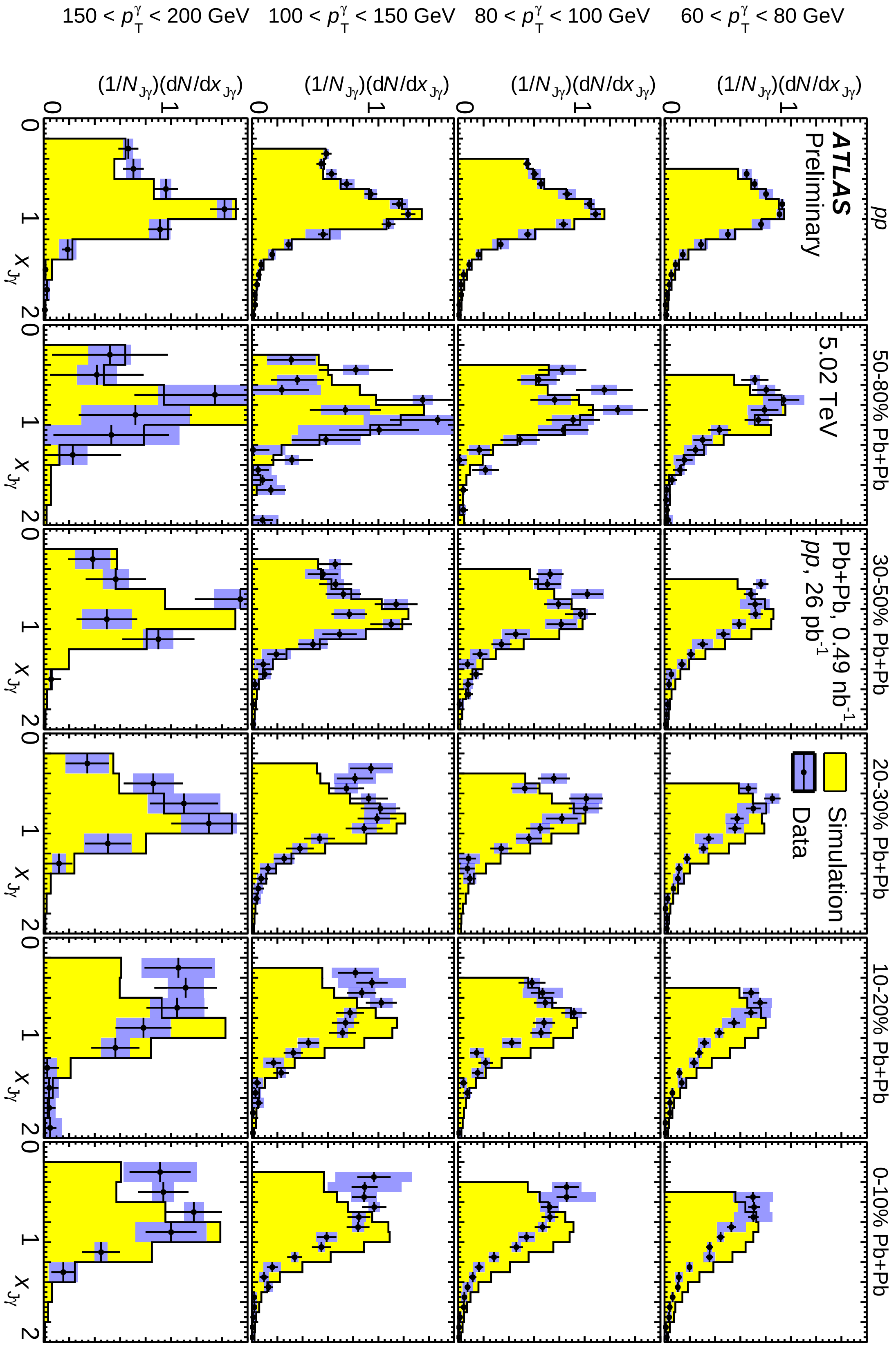

Figure 13: Overview of all measured $x_{J\gamma}$ results in *pp* and Pb+Pb data (markers) and simulation (histogram). The vertical bars and the shaded bands show the statistical and systematic uncertainties on the data, respectively. Each row and column are a different selection on p_{T}^{γ} and event class, respectively.

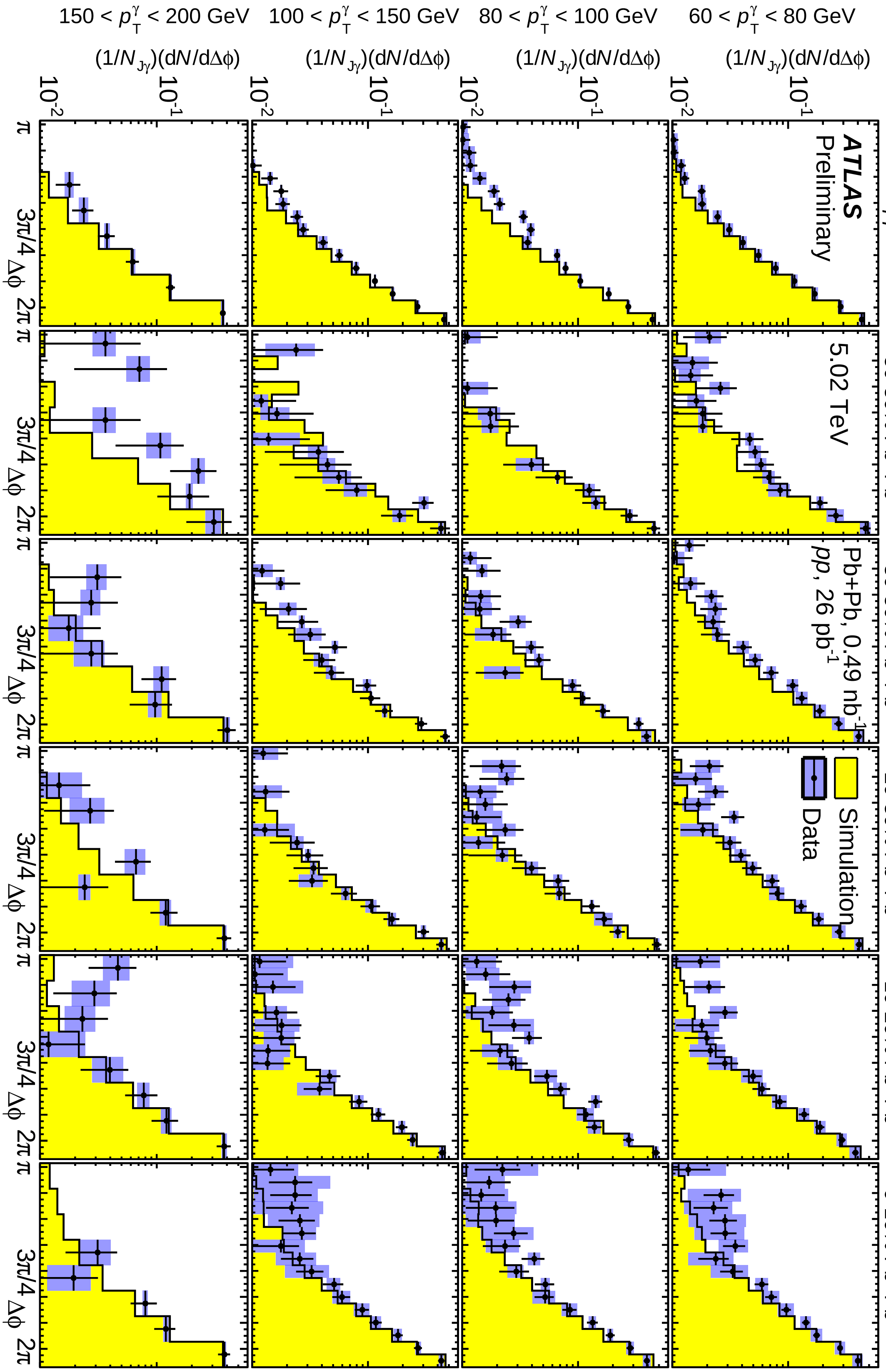

Figure 14: Overview of all measured $\Delta\phi$ results in pp and Pb+Pb data (markers) and simulation (histogram). The vertical bars and the shaded bands show the statistical and systematic uncertainties on the data, respectively. Each row and column are a different selection on p_{T}^{γ} and event class, respectively.